

Host-Guest Systems Based on Nanoporous Crystals

Edited by Franco Laeri, Ferdi Schüth, Ulrich Simon, Michael Wark
Invited by U. Simon

Wiley-VCH, Weinheim 2003. ISBN 3-527-30501-7

5 Electronic Structure of Zeolite-Stabilized Ions and Quantum Dots

Gion Calzaferri^{a*)}, Stephan Glaus^{a)}, Claudia Leiggener^{a)}, Ken'ichi Kuge^{b)}

^{a)} Department of Chemistry and Biochemistry,
University of Bern, Freiestrasse 3, CH-3000 Bern 9, Switzerland

^{b)} Faculty of Engineering, Chiba University, 1-33 Yayoi-cho, Inage-ku, Chiba 263, Japan

5. 1 Introduction

5.2 $H_8Si_8O_{12}$: A Model for the Vibrational and Electronic Structure of Zeolite A

5.3 Electronic Structure of Cu^+ , Ag^+ , and Au^+ -Loaded Zeolites

5.4 Electronic Structure of Ag^+ -Zeolite A

5.5 Quantum-Sized Silver Sulfide Clusters in Zeolite A

5.6 Intrazeolite Charge Transport

5.7 Conclusions

References

^{*)} gion.calzaferri@iac.unibe.ch

5. 1 Introduction

Zeolite materials can act as hosts for supramolecular organization of molecules, ions, complexes, clusters, and quantum sized particles. They allow the design of precise and reversible functionalities [1]. The possibility of arranging zeolite microcrystals of good quality and narrow size distribution as dense monolayers on different substrates can be used to realize distinct properties [2-7]. New electronic structures are accessible either by specific geometrical arrangements made possible by the structure of the host and/or by explicitly involving their electronic properties.

Three functionalities are of special importance in our research: *intrazeolite ion transport*, *intrazeolite charge transport*, and *intrazeolite excitation energy transport* (energy migration). The zeolite acts as a host which is not actively involved in the corresponding process, but provides the necessary geometrical and chemical environment. It can also lead to largely *improved chemical stability* of incorporated species by shielding them from chemicals with which they would otherwise react or by preventing intra molecular rearrangements due to the limited free space available. A number of methods have been developed for preparing zeolites containing the desired molecules, ions, complexes, or clusters. These are crystallization inclusion, ion exchange, incorporation from the gas phase, or in situ synthesis. Each of these methods has its advantages and disadvantages depending on the specific problem to be solved.

The most interesting phenomena seem to occur in micro- and nanometer sized crystals. Despite of the very fast progress of nanoscience techniques, the unambiguous experimental evidence for structure determination, for measuring intrazeolite charge transport or for the interpretation of photophysical phenomena is still difficult and time-consuming. An improved understanding of the electronic structure of these host-guest materials is therefore of decisive importance.

Especially for the synthesis of quantum confined semiconductor clusters such as CdS [8-12], CdSe [10], CdO [13], GaP [14], PbS [15], Se [16], Si [17, 18], SnO₂ [19], TiO₂ [13, 20], ZnO [13, 21, 22], ZnS [10, 11, 21], and ZnSe [10], different types of zeolites are used, because their cavities determine to a great extent the size and shape of the clusters. In this article, we focus on the framework of the zeolites A, Y, and L shown in Figure 1. These zeolites are crystalline aluminosilicates with cavity and channel structures. Their lattices are enormous polyanions which contain cations for charge compensation.

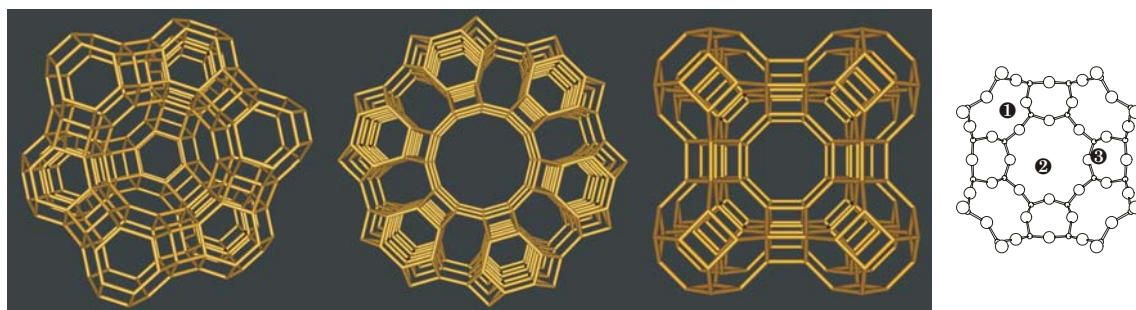


Figure 1. Structures of zeolite Y (left), zeolite L (middle), and zeolite A (right). The bridging oxygens are omitted. Cation positions in zeolite A 1) 6-ring, 2) 8-ring, and 3) 4-ring are shown on the right side.

In chapter 2 the electronic structure of a zeolite framework as derived from $\text{H}_8\text{Si}_8\text{O}_{12}$, as smallest cage molecule of relevant size and structure, is discussed. Chapter 3 points out the general idea of the electronic structure of Cu^+ , Ag^+ , and Au^+ loaded zeolites, while Ag^+ loaded zeolites are discussed in detail in chapter 4. We proceed with the synthesis and analysis of quantum sized clusters in the cavities of zeolites in chapter 5. These tunable semiconductor materials open a variety of fascinating phenomena. Chapter 6 points out the controversial topic of intrazeolite charge transport in the channels of zeolites and discusses the delicate part located at its interface. A new idea for solving the interfacial problem is reported. We end up with some conclusions in chapter 7.

5.2 $\text{H}_8\text{Si}_8\text{O}_{12}$: A Model for the Vibrational and Electronic Structure of Zeolite A

The framework of zeolite A can be generated by placing cubic T_8O_{12} double four rings (D4R) in the centers of the edges of 12.3 \AA length, connected by oxygen bridges. The center of the unit cell is a large cavity with a free diameter of about 11 \AA ; 8-membered rings with a free diameter of 4.1 \AA give access to the large cavity. The relation between the D4R and the zeolite structure is shown in Figure 2 on the right side. The bridging oxygens are omitted in the middle and upper part of this Figure, as usual in this kind of drawings. They have been added in the next step which leads to the $\text{H}_8\text{Si}_8\text{O}_{12}$ molecule. We have shown, that this molecule is an excellent model for studying properties not only of the D4R secondary building unit and thus of zeolite A, but also for advancing our understanding of aluminosilicate based zeolites in general, because it is easy to correlate the vibrational and the electronic structure of $\text{O}_h\text{-H}_8\text{Si}_8\text{O}_{12}$ with that of the hypothetical $\text{O}_h\text{-H}_{24}\text{Si}_{24}\text{O}_{36}$ [23-27]. The latter bears the structure of the sodalite cage which can be used as a link to many zeolites.

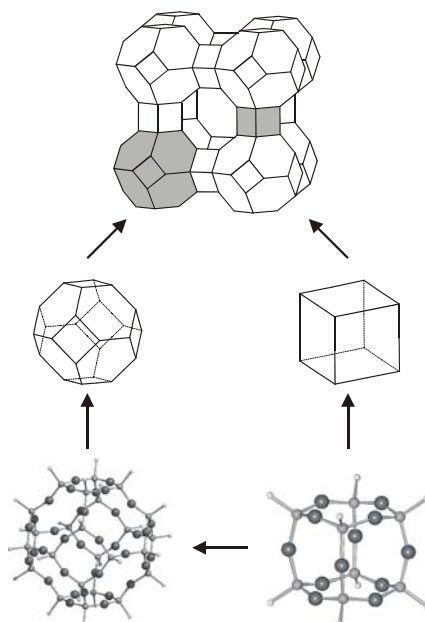


Figure 2. Relation between the structure of zeolite A and $\text{H}_8\text{Si}_8\text{O}_{12}$ (right) and $\text{H}_{24}\text{Si}_{24}\text{O}_{36}$ (left).

It is amazing that among the many orbitals of $\text{O}_h\text{-H}_8\text{Si}_8\text{O}_{12}$ there is exactly one of A_{2g} symmetry [28]. This pure oxygen-lone pair, which cannot interact with AOs from other

centers than oxygen, is the highest occupied orbital (HOMO), followed by a number of oxygen lone pairs between -10.75 eV and -11.7 eV which interact only slightly with the Si atoms. A comparison of the calculated one-electron energy levels in the HOMO region and the measured photoelectron spectrum is illustrated in Figure 3. The calculated first ionization energy of 10.7 eV is low but in good agreement with the experimental observation. To get a feeling for the consequences of this relatively high lying HOMO, we compare it with the first ionization energy of water which is 12.6 eV and attributed to the energy of the p-type oxygen lone pair of the water molecule [29]. We note that the first ionization energy of α -quartz is 10.4 eV, as determined by valence-band spectroscopy [30].

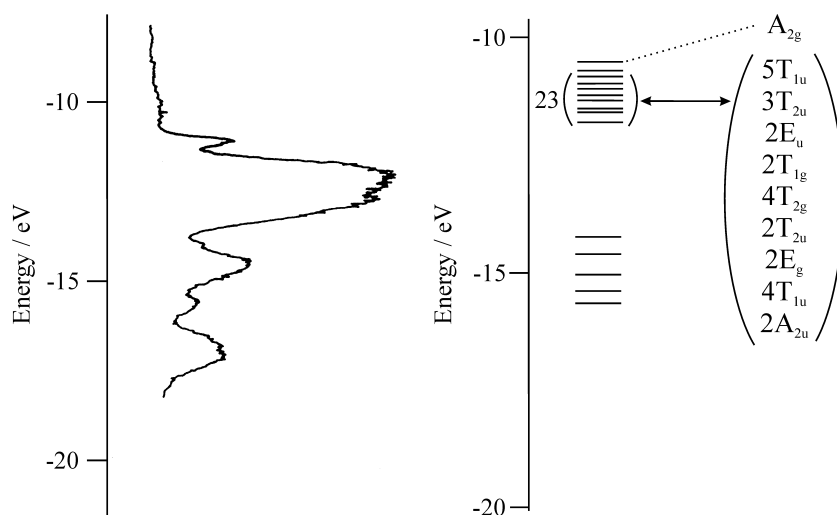


Figure 3. Photoelectron spectrum of $\text{H}_8\text{Si}_8\text{O}_{12}$ (left) and calculated occupied electron levels (right) [28].

The link of the electronic structure of $\text{H}_8\text{Si}_8\text{O}_{12}$ and that of zeolite A was discussed in Ref. [24]. The result of this is summarized in Figure 4, where we illustrate the band structure and density of states of the silicon dioxide analogue of zeolite A, which is especially simple because of the absence of co-cations. We observe that the bands in the HOMO region are flat which indicates the presence of non-bonding states. Some bands below -14 eV are significantly bent and contribute to the Si–O bonding. Further insight is gained from the density of states $\text{DOS}(E)$, defined in such way that $\text{DOS}(E)dE$ is the number of states in the interval E to $E+dE$. Since we are expressing the crystal orbitals as linear combination of atomic orbitals (LCAO) we can project out specific atomic orbitals or linear combinations of them. In Figure 4 this is done by shading the oxygen 2p contributions and leaving the 2s oxygen and the silicon contributions blank. This shows that the HOMO region consists of nearly pure oxygen 2p lone pairs which we denote as $|O\rangle$.

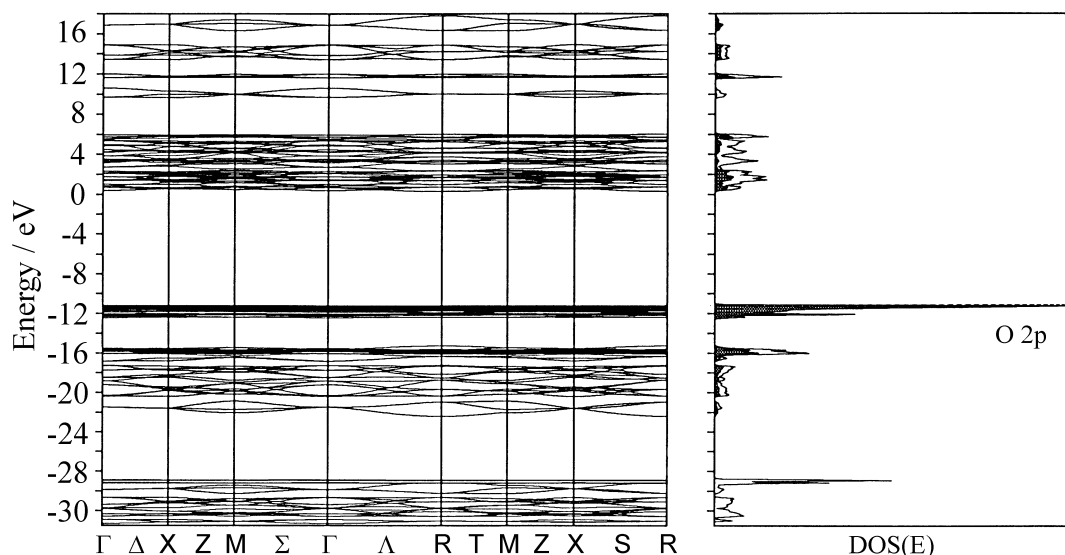


Figure 4. Band structure (left) and density of states (right) of the silicon dioxide analogue of zeolite A. The oxygen 2p density is projected out (shaded regions).

5.3 Electronic Structure of Cu^+ , Ag^+ , and Au^+ -Loaded Zeolites

The Al^{3+} centers in zeolites cause a negatively charged framework (AlO_2^-). This charge is compensated by exchangeable cations, which influence the band structure to some extent. It is, however, reasonable to assume that the HOMO and the LUMO regions are in general similar to those illustrated in Figure 4. Provided this is correct, we can guess that the HOMO-LUMO region of zeolites containing monovalent cations of the type Li^+ , ..., Cs^+ , Cu^+ , Ag^+ , Au^+ can be drawn qualitatively as illustrated in Figure 5. It consists of the oxygen lone pair region denoted as $|\text{O}\rangle$, the empty ns' level of the metal cations M^+ , and of the LUMO region of the zeolite which may be modified by np' contributions of M^+ . The ns' and np' levels are modified to some extent with respect to the ns and np levels of the free cations by their interaction with the surrounding [31-34]. This scheme suggests the occurrence of ligand to metal charge transfer (LMCT) transitions of the $ns' \leftarrow |\text{O}\rangle$ type, exciting an oxygen lone pair electron to the metal cation coordinated to the zeolite oxygen. The energy ΔE_{CT} needed for this transition is equal to the difference of the ionization potential $\text{Ip}_{|\text{O}\rangle}$ of the oxygen lone pair and the first ionization potential Ip_{M} of the metal M , plus a correction Δ which stands for the antibonding interaction of the empty ns' level of the metal ion M^+ with the environment.

$$\Delta E_{\text{CT}}(ns' \leftarrow |\text{O}\rangle) = \text{Ip}_{|\text{O}\rangle} - \text{Ip}_{\text{M}} + \Delta \quad (1)$$

This simple relations allows us to estimate the energy of the charge transfer band for different situations. We do this in Table 1 for cations in water and in a silicate with oxygen lone pairs at about -10.7 eV, as discussed in the previous section.

Cations	I_{pM} / eV	$\Delta E_{CT}(ns' \leftarrow O\rangle) - \Delta / \text{cm}^{-1}$	
		$I_{p O\rangle} = 12.6 \text{ eV}$	$I_{p O\rangle} = 10.7 \text{ eV}$
Li	5.3600	56'216	43'067
Na	5.1200	60'326	44'183
K	4.3200	66'778	51'454
Rb	4.1600	68'078	52'745
Cs	3.8700	70'407	55083
Cu	7.6800	39'679	24'356
Ag	7.5400	40'808	25'485
Au	9.1800	27'582	12'258

Table 1: Estimation of the $ns' \leftarrow |O\rangle$ LMCT charge transfer transition energy ΔE_{CT} for the cations M^+ in water and in a silicate with $I_{p|O\rangle} = 12.6 \text{ eV}$ and 10.7 eV , respectively.

$ns' \leftarrow |O\rangle$ charge transfer transitions have been observed in $\text{Cu}^+ \text{---} \text{A}$, $\text{Cu}^+ \text{---} \text{X}$ and $\text{Ag}^+ \text{---} \text{A}$ zeolites in the region of $28'000 \text{ cm}^{-1}$. This means that Δ is in the order of 0.5 eV or $4'000 \text{ cm}^{-1}$ for these transitions. CT transitions for which Δ is larger will be discussed in the next section. Ag^+ in water absorbs light at about 225 nm [35], in agreement with Eq. (1). Table 1 shows that Au has the largest I_{pM} , which gives Au its noble character. In general Au^+ is unstable but can be stabilized by specific ligands. This makes it difficult to incorporate Au^+ by conventional ion-exchange methods. However, some researchers reported the synthesis of Au^+ loaded zeolites by means of ion exchange with gold complexes or by sublimation of $(\text{AuCl}_3)_2$ [36]. The electronic spectra of the resulting materials reported so far suggested that Au^+ was still coordinated to chloride and direct interaction to the zeolite could not be observed. Clear assignment of the nature of the observed electronic transitions are not established. More work is needed to get electronic spectra of Au^+ coordinated to zeolite oxygen atoms. We should also add that it is still difficult to locate the ns levels of divalent cations such as Ca^{2+} ($I_{p1} = 6.01 \text{ eV}$, $I_{p2} = 11.82 \text{ eV}$) and Mg^{2+} ($I_{p1} = 7.61$, $I_{p2} = 14.96$) in zeolites. We must leave their position and properties open at present time.

Luminescence of the $\text{Cu}^+ \text{---} \text{A}$ [31], $\text{Cu}^+ \text{---} \text{X}$ [32], $\text{Cu}^+ \text{---} \text{ZSM5}$ [37, 38], and $\text{Ag}^+ \text{---} \text{A}$ zeolites after $ns' \leftarrow |O\rangle$ excitation occurs at $400\text{--}700 \text{ nm}$, depending on the samples and the conditions. This means that the Stokes shift is in the order of 8000 cm^{-1} . Excitation of an electron from the oxygen lone pair level $|O\rangle$ into the empty ns' orbital of the metal cation causes a formal reduction of M^+ to M^0 . The radius r of M^+ is significantly smaller than that of M^0 ($r(\text{Cu}^+) = 0.96 \text{ \AA}$, $r(\text{Cu}^0) = 1.35 \text{ \AA}$, $r(\text{Ag}^+) = 1.26 \text{ \AA}$, $r(\text{Ag}^0) = 1.6 \text{ \AA}$). This means that the LMCT transition blows up the metal by $0.3\text{--}0.4 \text{ \AA}$ which causes a change in its position. As a consequence, the ns' level relaxes to a state of lower energy which we denote as $(|O\rangle)^\oplus(ns')^1$ state. The latter relaxes to the ground state either by emitting a photon with a large Stokes shift or by radiationless processes, as illustrated in Figure 5 on the right side.

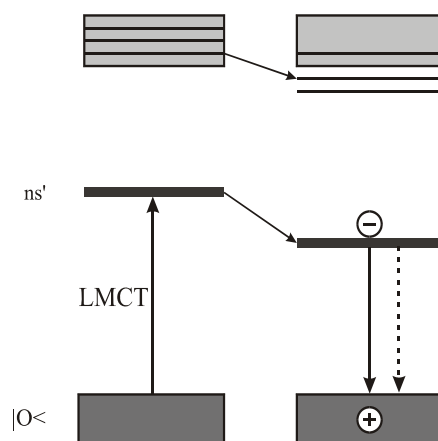


Figure 5. Energy diagram of a metal cation in a zeolite framework. The HOMO region consists of many narrow lying localized states strongly concentrated on the oxygen atoms. We call this region lone pair region of the silicate and abbreviate it as $|O<$. Some of the np' levels may reach into the LUMO region of the silicate. Three lines have been added to indicate this.

5.4 Electronic Structure of Ag^+ -Zeolite A

Rálek et al. reported in 1962 that hydrated colorless zeolite $Ag^+_xNa^{+12-x}A$ turns yellow to brick-red on activation [39]. No explanation of this phenomenon was given at that time. Later it was believed that the color change was due to formation of silver clusters (Ag^0_n) in the cavities of silver zeolite A. These neutral silver species were assumed to form at elevated temperatures via an auto-reduction process in which O_2 from the zeolite framework was released [40]. We studied the vibrational spectra of Ag^+ zeolite A materials in some detail [41, 42], and we recently showed that activation at room temperature under high vacuum is already sufficient to produce the yellow form of $Ag^+_xNa^{+12-x}A$. The fully reversible color change, which depends on the hydration state of the silver zeolite, was attributed to electronic charge transfer transitions from the oxygen lone pairs of the zeolite framework to the empty 5s orbital of the Ag^+ ions, denoted as $Ag^+(5s) \leftarrow O(n)$ [33]. Pure sodium ($Na^{+12}A$) and calcium zeolite A (Ca^{2+}_6A) are colorless in both their hydrated and their activated (dehydrated) states. Silver containing sodium zeolite A is colorless in its fully hydrated form. In activated silver zeolite A materials, the Ag^+ is forced to coordinate zeolite oxygen because an insufficient number of water molecules are available. The question remained if specific coordination sites which act as yellow and/or red „color centers” can be identified. We answered this question by studying the UV/vis spectra of $Ag^+_xNa^{+12-x}A$ and of $Ag^+_xCa^{2+}_{6-0.5x}A$ materials in their fully hydrated, in HV room temperature dehydrated, and in HV elevated temperature dehydrated states. A comparison of such spectra is shown in Figure 6. The marked site preference of the ions in $Ag^+_xCa^{2+}_{6-0.5x}A$, probed by gas adsorption experiments, offered the unique possibility of investigating different coordination sites of Ag^+ ions in zeolite A [34]. Pure sodium and calcium zeolite A do not absorb light within the spectral range from $50'000 - 10'000 \text{ cm}^{-1}$ we have investigated. This means that any absorption band or colors observed in silver zeolite A materials are due to the presence of silver ions.

We found that 6- and 8-ring coordinated Ag^+ give rise to electronic transitions in the near UV region. An absorption in the visible, namely at $22'000 \text{ cm}^{-1}$, was only observed in materials where 4-ring coordinated Ag^+ was present and only they showed the typical deep yellow color. We also observed that Ag^+ avoids the 4-ring sites as long as possible in

$\text{Ag}^+_x\text{Ca}^{2+}_{6-0.5x}\text{A}$, namely as long as x is smaller than 10. In the case of $\text{Ag}^+_x\text{Na}^{+12-x}\text{A}$ either a Na^+ or a Ag^+ is forced to coordinate a 4-ring site because all other places are occupied. The presence of the $22'000\text{ cm}^{-1}$ absorption responsible for the yellow color, already at $x < 0.2$, proves that isolated Ag^+ ions are sufficient to cause it and that the 4-ring coordination of Ag^+ is significantly stronger than that of the Na^+ . The red color of elevated temperature activated samples is caused by a strong absorption band at $19'000\text{ cm}^{-1}$. We observed that samples which remained colorless after room temperature activation never turned red, that samples with lower silver content than one Ag^+ per α -cage never turn red, and that room temperature dehydration under our experimental conditions was not sufficient to produce red colored samples. These observations strongly indicate that only samples with 4-ring coordinated Ag^+ can give rise to the $19'000\text{ cm}^{-1}$ band and this only if a second Ag^+ is not too far away at a 6-ring site, so that they can interact to develop a corresponding low lying state.

Molecular orbital calculations carried out on a sufficiently large zeolite part consisting of 1296 atoms allowed us to address questions about the nature of the HOMO and of the LUMO region, about the contributions of the zeolite framework atoms to the electronic transitions, about the influence of the local symmetry of the Ag^+ at 4- and at 6-ring sites, and about the importance of $\text{Ag}^+—\text{Ag}^+$ interactions. In order to avoid geometries without experimental relevance, we restricted this study to Ag^+ at 4- and 6-ring sites known from x-ray measurements.

We found that the occupied frontier orbital region consists mainly of two bunches of levels: the HOMO region from about -11 eV to -12.6 eV and the next levels below -13.6 eV . The LUMO consists of a single level of mainly $\text{Ag}^+(5s)$ character. The LUMO+1 was found to be energetically too high to be of relevance in this study. Thus, the oscillator strength of transitions from the first 1244 levels to the LUMO were calculated. For 6-ring coordinated Ag^+ all levels in the HOMO region derive from mostly non-interacting oxygen lone pairs which we abbreviate as $\text{O}(n)$. The LUMO is a rather pure $\text{Ag}^+(5s)$ with some contribution from the three coordinating oxygens. Thus, all electronic excitations in question are ligand-to-metal charge-transfer transitions (LMCT) from oxygen lone pairs to the silver ion. They are energetically located in the near UV and depend only little on the polarization. The agreement in shape and position between the computed spectrum and the experiment allowed us to conclude that a 6-ring coordinated Ag^+ gives rise to electronic transitions from zeolite oxygen lone pairs to the $\text{Ag}^+(5s)$ orbital in the near UV. We denote such electronic transitions as $\text{Ag}^+(5s)\leftarrow\text{O}(n)$ [34].

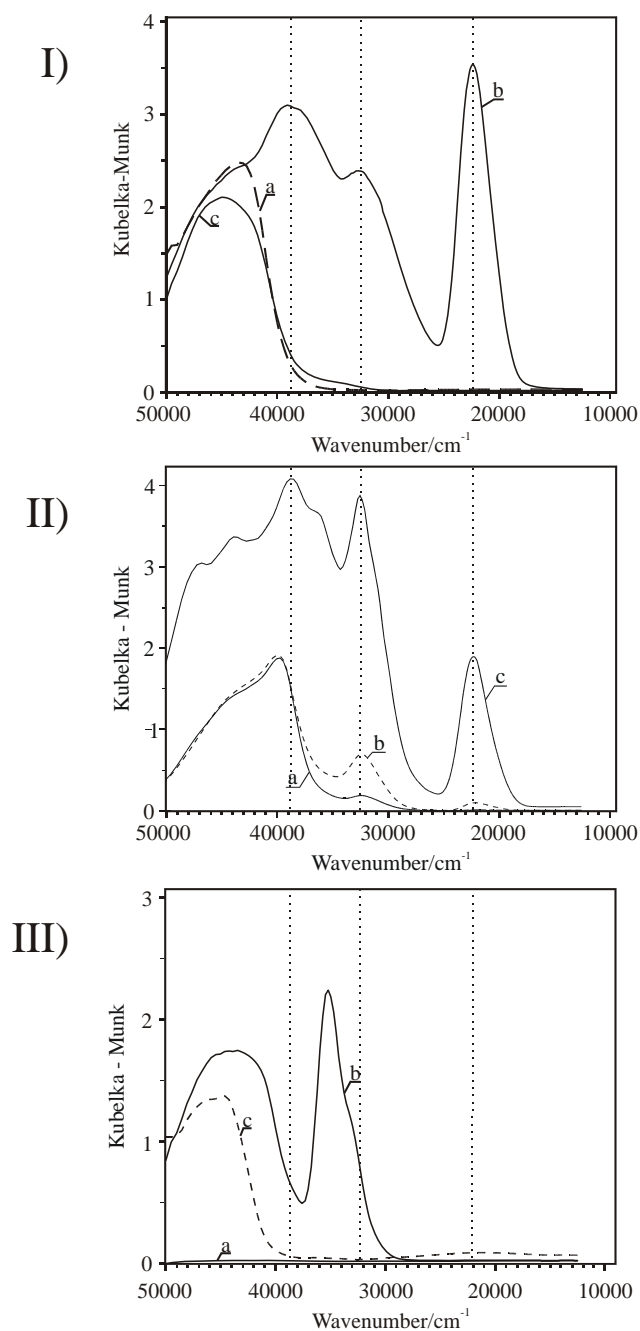


Figure 6. I) UV/vis spectra of $\text{Ag}^+\text{Na}_6\text{A}$: a) freshly exchanged, never activated; b) activated at room temperature; c) activated at room temperature and exposed to pure water vapor before measurement. II) UV/vis spectra of various silver containing zeolites activated at room temperature: a) $\text{Ag}^+\text{Ca}^{2+}_1\text{A}$; b) $\text{Ag}^+\text{Ca}^{2+}_{0.5}\text{A}$; c) Ag^+A . III) UV/vis spectra of zeolite Y: a) Na^+Y , b) Ag^+Y , activated at room temperature, c) the same as b) but after exposure to moisture [34].

The bands of the 4-ring coordinated Ag^+ are strongly polarized. Two almost degenerate low-energy absorption bands and a prominent high-energy band dominate the spectrum. The first one can be described as an $\text{Ag}^+(5s) \leftarrow \text{O}(n)$ LMCT transition. It is responsible for the yellow color. The near UV band exhibits some $\text{Ag}^+(5s) \leftarrow \sigma$ character but it can still be regarded as an oxygen to silver LMCT transition. It is natural to assign it to the $32'000 \text{ cm}^{-1}$ band shown in Figure 6 (I and II). Interestingly, out of the 1244 electronic

transitions from the frontier orbital region to the LUMO only three bear significant intensity. This clearly demonstrates the paramount importance of oscillator strengths and how problematic an estimation of electronic spectra based on DOL arguments alone can be. We conclude that the calculated $\text{Ag}^+(5s) \leftarrow \text{O}(n)$ transition of 4-ring coordinated Ag^+ is in agreement with the appearance of a deep yellow color of room temperature activated Ag^+ containing zeolite A materials with occupied 4-ring positions in the sodalite cavity. The main difference between the 4-, 6- and 8-coordinated Ag^+ is that the antibonding interaction of the $\text{Ag}^+(5s)$ orbital with the oxygen lone pair is weaker in the 4-ring position and larger in the other positions.

6-ring coordinated Ag^+ give rise to electronic transitions in the near UV and the 4-ring coordinated Ag^+ is responsible for the deep yellow color of the room temperature activated material. This implies that similar $\text{Ag}^+(5s) \leftarrow \text{O}(n)$ LMCT transitions are to be expected in other Ag^+ exchanged zeolites. Ag^+ exchanged zeolite Y can be used as a test. We therefore report in Figure 6, bottom UV/vis spectra of (a) pure Na^+_{69}Y , (b) room temperature HV dehydrated Ag^+_{69}Y , and (c) the same as (b) after exposure to moisture. The main result is that an intense band at about $34'000 \text{ cm}^{-1}$ appears upon dehydration which vanishes upon rehydration. By analogy one would also expect a similar type of LMCT transitions in Cu^+ zeolite materials. $\text{Cu}^+(4s) \leftarrow \text{O}(n)$ LMCT transitions, reversible upon HV hydration/dehydration, have indeed been observed in Cu^+ zeolite A and X [31, 32].

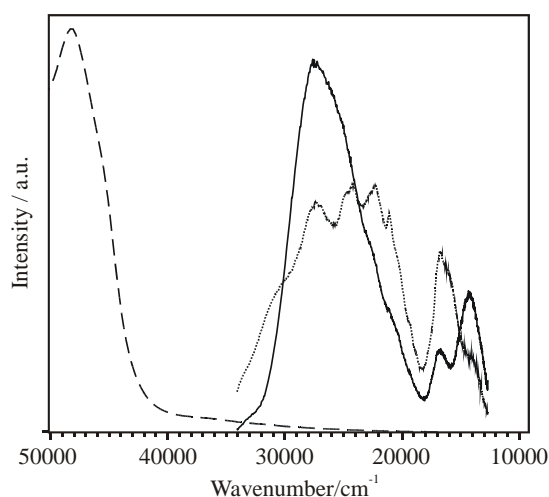


Figure 7 Luminescence spectra at -195°C (solid line) and at room temperature (dotted line), excited at 250 nm, and diffuse reflectance spectrum (dashed line, Kubelka-Munk) of $\text{Ag}^+_{1}\text{Ca}^{2+}_{5.5}\text{A}$.

The luminescence properties of Ag^+ -loaded zeolites depend on the amount of water which is available for coordination to the silver ions. $\text{Ag}^+_x\text{Ca}^{2+}_{6-0.5x}\text{A}$ shows luminescence even in the fully hydrated state while in the case of $\text{Ag}^+_x\text{Na}^+_{12-x}\text{A}$ luminescence can only be observed in partially hydrated states [42]. Because of the stronger electrostatic interaction between water and Ca^{2+} than between water and monovalent cations most of the water molecules in the hydrated zeolite are coordinated to Ca^{2+} and only a few of them are coordinated to Ag^+ . If there are only monovalent cations like in $\text{Ag}^+_x\text{Na}^+_{12-x}\text{A}$ materials the number of water molecules which coordinate to Ag^+ is larger than in $\text{Ag}^+_x\text{Ca}^{2+}_{6-0.5x}\text{A}$ samples. Thus the condition for luminescence of Ag^+ -loaded zeolite A is that only a small number of

water molecules coordinate to the silver ions. Figure 7 shows the absorption and the luminescence spectra of fully hydrated $\text{Ag}^+_1\text{Ca}^{2+}_{5.5}\text{A}$. The luminescence intensity is enhanced by cooling the sample with liquid nitrogen.

Based on all the information which has been collected over the last few years, we can now draw the schematic state diagram in Figure 8 for Ag^+ containing zeolites.

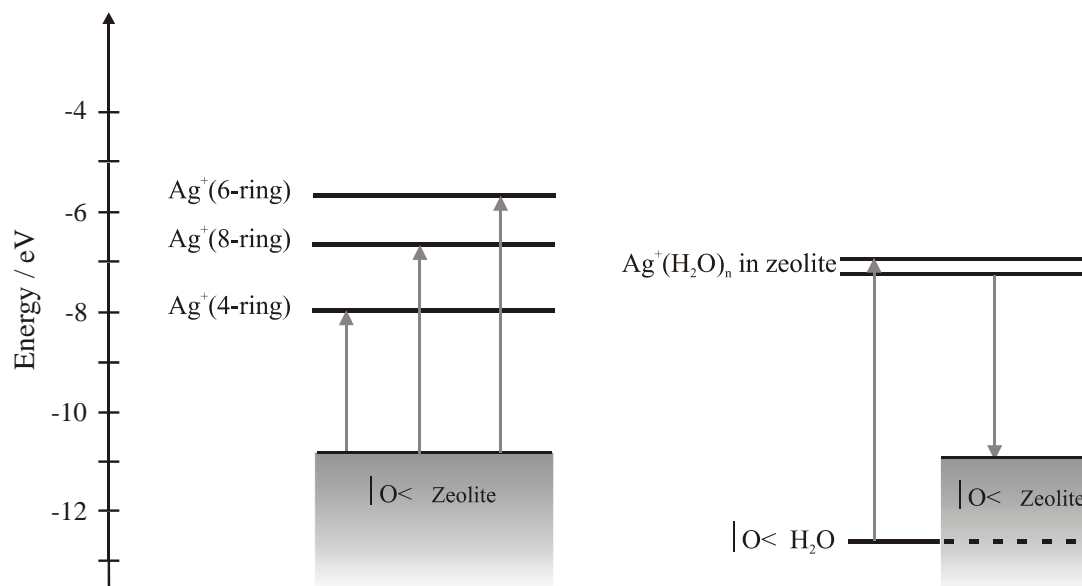


Figure 8 Frontier orbital state diagram of Ag^+ -loaded zeolite A. On the left side we show the levels observed in room temperature activated zeolites in which all three sites are occupied by silver ions, while the scheme on the right side corresponds to situations typically observed in $\text{Ag}^+_x\text{Ca}^{2+}_{6-0.5x}\text{A}$ materials containing some water.

5.5 Quantum Sized Silver Sulfide Clusters in Zeolite A

The synthesis and the properties of semiconductor particles in the size regime of a few up to hundreds of angstroms continues to attract considerable interest [43]. Significant quantum confinement effects can be observed in clusters made from II–VI or IV–VI compounds such as CdS [44], CdSe [45], ZnO [46], ZnS [47], or PbS [48]. While excellent progress has been made in the preparation and characterization of these materials, very little is known about the properties of small Ag_2S species. This can be partly attributed to the fact that silver sulfide clusters show a strong tendency to aggregate into bulk, which complicates their synthesis considerably. The well-defined cavities of zeolites provide a convenient environment for preparing clusters with a narrow size distribution or even cluster arrays [9]. We have shown, that the framework of zeolite A and ZK4 prevents the silver sulfide clusters from aggregating and we reported the synthesis and the optical absorption and emission spectra of silver sulfide zeolite A composites. The preparation method is based on the observation discussed in section 4 that Ag^+ -loaded zeolite A can be reversibly activated at room temperature [49-52].

The low-temperature phase of bulk silver sulfide is stable up to approximately 177 °C and is usually denoted as $\alpha\text{-Ag}_2\text{S}$. Historically, we can go as far back as 1833 when Michael Faraday made the remarkable discovery that silver sulfide behaves as an insulator at room temperature but exhibits high electrical conductivity at elevated temperatures, leading him to

the following conclusion:[53] *"There is no other body with which I am acquainted, that, like sulphuret of silver, can compare with metals in conducting power for electricity of low tension when hot, but which, unlike them, during cooling, loses in power, whilst they, on the contrary, gain. Probably, however, many others may, when sought for, be found."* Today it is well known that α -Ag₂S is a semiconductor with a monoclinic structure [54] and a band gap of approximately 1 eV at room temperature [46]. Figure 9 on the left shows the calculated density of states (DOS) of bulk α -Ag₂S. The electronic transition from valence band to conduction band is essentially a charge transfer from 3p(S) to 5s(Ag). This property is also observed in a Ag₂S molecule. The HOMO–LUMO region of such a molecule, and presumably also of larger silver sulfide clusters, fits well into the gap between the oxygen lone pairs of zeolite A and the zeolite A LUMO region (see right side of Figure 9), therefore giving rise to a variety of electronic transitions [49].

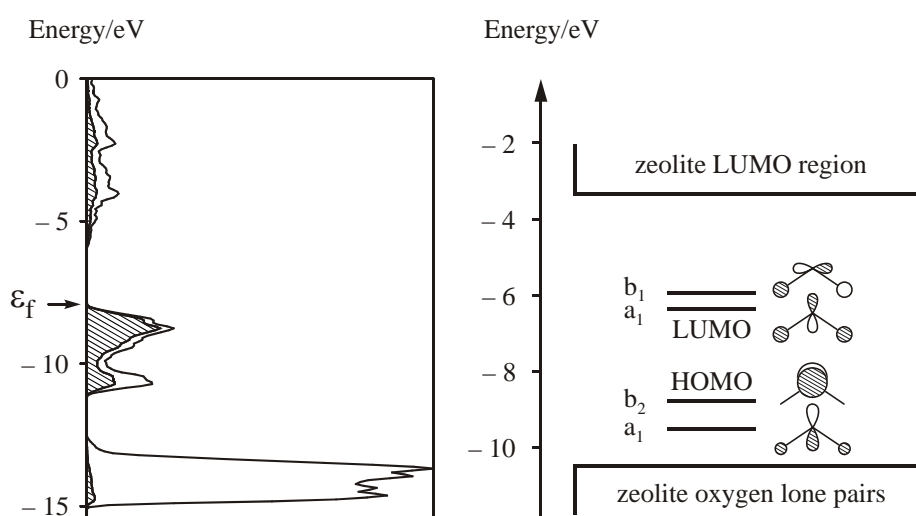


Figure 9. Left: Density of states (DOS) plot of α -Ag₂S. The hatched region indicates the contribution of sulfur 3p-states. The Fermi level ϵ_f is marked by an arrow. Right: HOMO–LUMO region of a Ag₂S molecule in comparison to the HOMO–LUMO region of zeolite A [49].

Bulk silver sulfide has been considered for photoimaging and photodetection in the IR [55], while small clusters are known to play an important role in photographic sensitivity [56–59]. It has been reported that silver sulfide clusters with sizes ranging from 23 Å to 76 Å can be synthesized in reverse micelles [60]. Another method utilizes the rapid expansion of a AgNO₃ solution in supercritical ammonia into an ethanol solution of Na₂S. An average diameter of 73 Å was found after stabilizing the thus formed particles with a suitable polymer [61]. Dosed addition of a AgNO₃ solution to a gelatin solution containing Na₂S was reported to yield silver sulfide clusters in the size regime between 30 Å and 100 Å [62]. Other methods use nylon thin films (cluster size ranging from 47 Å to 112 Å) [63], Nafion membranes (cluster size ranging from 50 Å to 150 Å) [64] or capping with cysteine/glutathione (average cluster size of 90 Å) [65] to stabilize the silver sulfide clusters. Some of the results obtained by the above mentioned methods suggest the presence of a quantum size effect for silver sulfide clusters with a diameter between 20 Å and 100 Å (see Refs. [61, 62, 65, 66]), while other reports clearly negate the presence of such an effect (see e.g. Ref. [63]).

The synthesis of silver sulfide particles in the cavities of zeolite A in the size regime below 15 Å can be divided into four steps: (i) loading of the zeolite with Ag⁺, (ii) activation of the Ag⁺-loaded zeolite, (iii) reaction with H₂S, and (iv) rehydration. To explain the mechanism of cluster growth we start by examining the formation of silver sulfide clusters in zeolite samples with a low content of Ag⁺, e.g. 0.05 Ag⁺ per α-cage. The silver ions are evenly distributed among the α-cages, implying that 5 % of them actually contain a silver ion in this case (see Figure 3 in Ref. [33]). Activation of the Ag⁺-loaded zeolite and subsequent adsorption of H₂S leads to reaction (2) inside an α-cage. The formation of protons can easily be observed.



It can be assumed that the silver atom of the thus formed AgSH molecule is at this stage still coordinated to zeolite framework oxygen atoms. Uptake of water during rehydration mobilizes the AgSH molecules through solvation. Encounter of two AgSH molecules causes the following reaction:



H₂S escapes from the zeolite. The equilibrium (3) is shifted to the right if the H₂S is removed. The reaction can be reversed in presence of H₂S. Further diffusion of the Ag₂S molecules has not been observed so far [51, 52].

In our first communication, we reported the luminescence spectra of Ag₂S–NaA samples [49]. Ag₂S–CaA samples were found to exhibit comparatively much stronger luminescence, usually well visible at room temperature. Figure 10 shows the luminescence spectra of Ag₂S–CaA samples with varying silver sulfide content. The stoichiometry of the silver sulfide zeolite A composites is Ag_xS_{x/2}Na_{12-x}H_xSi₁₂Al₁₂O₄₈*nH₂O for clusters in NaA and Ag_xS_{x/2}Ca_{6-x/2}H_xSi₁₂Al₁₂O₄₈*nH₂O for clusters in CaA (pseudo unit cell contents). We will use the abbreviations Ag₂S–NaA-x and Ag₂S–CaA-x for the differently loaded samples, where x denotes the number of silver ions per α-cage of zeolite A.

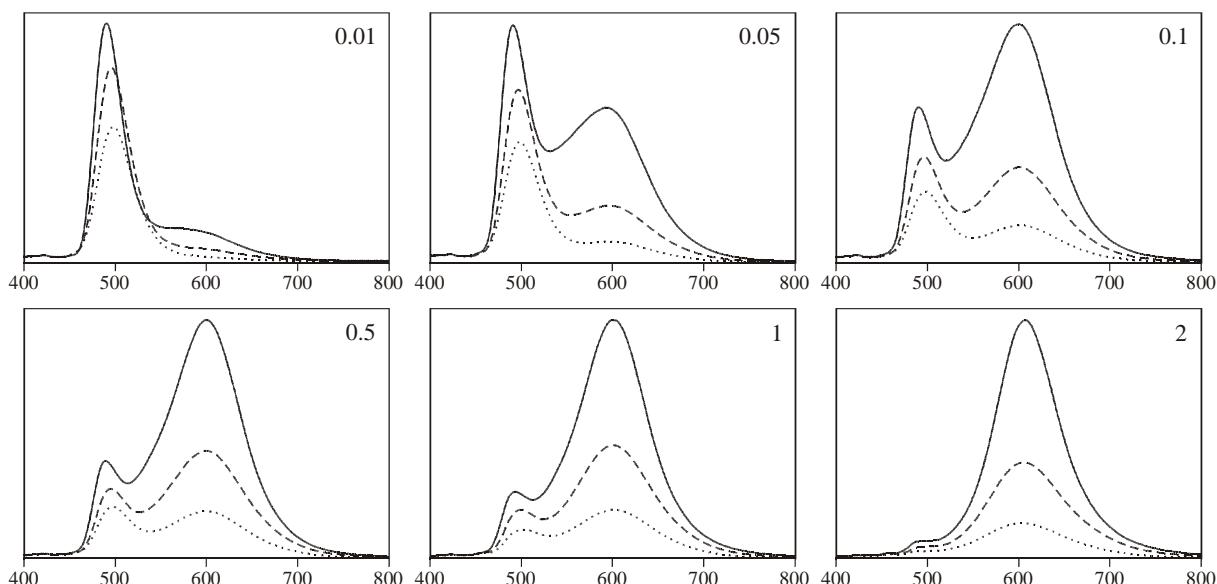


Figure 10. Luminescence spectra of Ag₂S–CaA-x samples (x = 0.01, 0.05, ... 2) at –195 °C (solid lines), –100 °C (dashed lines) and –50 °C (dotted lines). The abscissa and the ordinate give the wavelength in nanometers and the emission intensity, respectively. Excitation was performed at 280 nm [51].

Comparison of the spectra shown in Figure 10 with the spectra of Ag_2S –NaA samples reported in Ref. [49] reveals the following similarities: A low silver sulfide content is characterized by a blue-green luminescence (480 nm for Ag_2S –NaA and 490 nm for Ag_2S –CaA) and a corresponding excitation spectrum with distinct and narrow bands. The Stokes shift is 1.3 eV. Given the distinct nature of the excitation bands and the low silver sulfide content, we conclude that the blue-green luminescence is caused by monomers of Ag_2S . Further evidence for this is reported in Ref. [52]. At higher loading levels, an orange-red luminescence becomes increasingly dominant.

By using CaA as host material it is possible to produce luminescent samples with silver sulfide content up to at least Ag_2S –CaA-6. Figure 11 shows the low-temperature luminescence spectra of Ag_2S –CaA-2, Ag_2S –CaA-4 and Ag_2S –CaA-6. These samples only exhibit the long wavelength emission, which is red-shifted with increasing silver sulfide content. This effect is accompanied by a shortening of the luminescence lifetime. The following average decay times were measured for Ag_2S –CaA- x samples at -160 °C: 81 μs ($x = 2$), 49 μs ($x = 3$), 26 μs ($x = 4$), 9 μs ($x = 5$), and 2 μs ($x = 6$). The mechanism that causes this increased quenching at high loading levels is not yet understood.

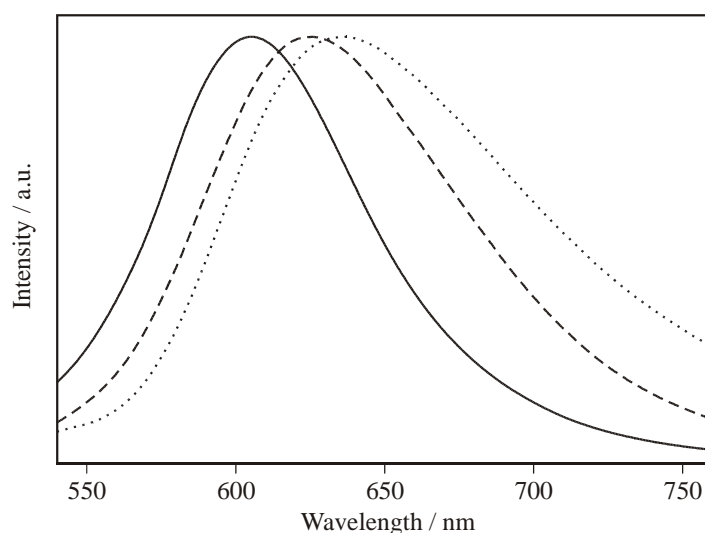


Figure 11. Luminescence spectra of Ag_2S –CaA-2 (solid), Ag_2S –CaA-4 (dashed) and Ag_2S –CaA-6 (dotted) at -195 °C. Excitation was performed at 280 nm. The spectra are scaled to identical heights.

The calculated electronic absorption spectrum of the Ag_2S monomer is essentially composed of 4 transitions between 300 and 400 nm, while the spectrum of AgSH features a single prominent transition at 276 nm. The NaSH monomer is found to absorb at even shorter wavelengths. This is in agreement with the assignment of the experimentally observed bands in the diffuse reflectance spectra of H_2S -loaded NaA and the Ag_2S –NaA samples. The HOMO of the Ag_2S , AgSH and NaSH monomers is essentially a $3p(\text{S})$ orbital. The electronic transition from this orbital to the corresponding LUMO generally features oscillator strengths smaller than 0.05. We expect that those transitions are difficult to observe in diffuse reflectance spectra, but they are essential for the luminescence behavior of the composites. In the case of the Ag_2S monomer the calculated HOMO–LUMO transition is found at 505 nm. This corresponds well to the blue-green luminescence observed in Ag_2S –NaA- x and Ag_2S –CaA- x samples of low silver sulfide content. The nature of the HOMO–LUMO transition is most likely maintained in larger silver sulfide clusters. This explains the

significant Stokes shifts which can be observed in the excitation and emission spectra (see Figures 5 and 6 in Ref. [51]) and the comparatively long luminescence lifetimes.

How does the electronic absorption spectrum of a Ag_2S monomer change upon interaction with another Ag_2S monomer, thus forming a Ag_4S_2 cluster? To answer this question, we first have to address the characteristics of this interaction. The appropriate interaction geometry for the two monomers is not immediately evident, mainly because of the yet unknown structure of Ag_4S_2 . Starting from the structures proposed by Bagatur'yants et al. [67], we selected the geometry possessing the highest symmetry, namely D_{2d} . Interaction was studied by reducing the distance between the two Ag_2S monomers. Figure 12 shows the corresponding correlation diagram. While the b_1 and b_2 levels of the monomers are little affected upon interaction, splitting of the two a_1 levels (LUMO and HOMO-1) into levels of b_2 and a_1 symmetry is observed. The thus formed a_1 orbitals are stabilized with respect to the corresponding orbitals in the isolated monomers, while the b_2 orbital that is generated from the HOMO-1 is destabilized. The energy of the b_2 orbital, which is formed upon splitting of the LUMO is only slightly affected by an alteration of the Ag_2S - Ag_2S distance. The increasingly antibonding s-s and p-p interaction is in this case compensated by an increasingly bonding s-p interaction. The splitting of the a_1 levels upon interaction leads to a red-shift of the electronic absorption and luminescence bands (note the reduction of the HOMO-LUMO gap) [51].

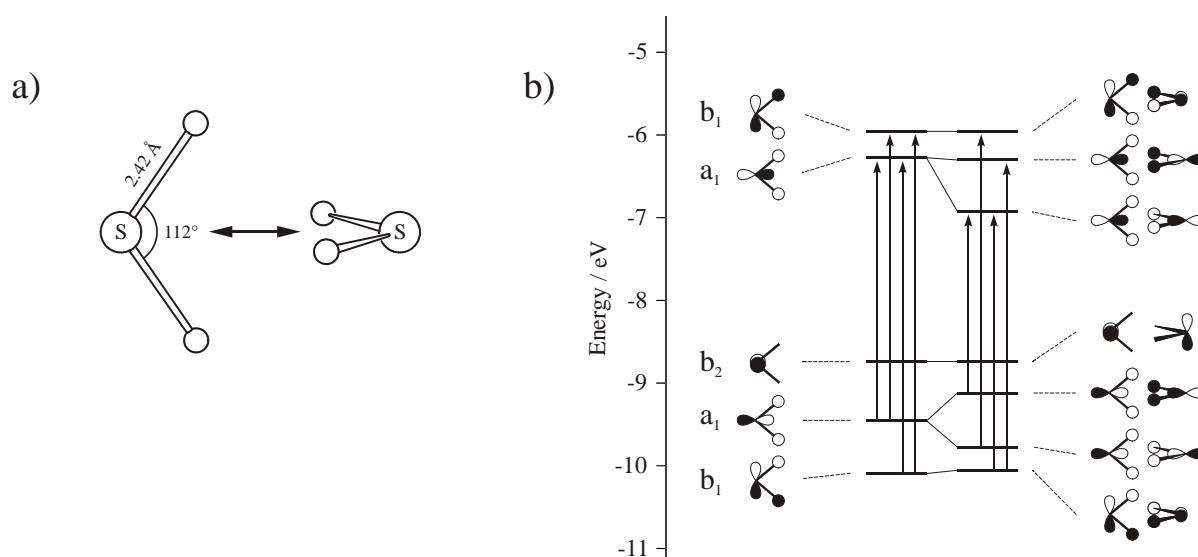


Figure 12. a) Scheme of the used structure for Ag_4S_2 . b) Frontier orbital correlation diagram of Ag_2S (left) and Ag_4S_2 (right). The contribution of the d orbitals to the molecular orbitals is marginal in this energy region and therefore not shown. Electronic transitions with an oscillator strength larger than 0.01 are indicated by arrows. The HOMO of Ag_2S and also of Ag_4S_2 is located at -8.7 eV.

When dealing with three-dimensional cluster arrays such as the Ag_2S - NaA -x and Ag_2S - CaA -x composites the question arises whether the properties of these materials are due to crystal effects originating from interacting clusters. We evaluated the relevance of such effects by calculating the density of states (DOS) of Ag_4S_2 clusters, which are arranged in a cubic lattice. The MO diagram of the Ag_4S_2 cluster used for this purpose is depicted in Figure 12 (right side) at an S-S distance of 5.6 Å. The development of the DOS upon variation of

the lattice constant is shown in Figure 13. Significant changes can be observed when the lattice constant is smaller than 10 Å. The bandgap decreases at values below 9 Å and disappears at 7.5 Å. The distance between the centers of two α -cages in zeolite A is 12.3 Å [68]. The model therefore predicts that there is no through space interaction between the clusters over the whole zeolite crystal up to a loading level of 4 Ag^+ per α -cage. The properties of $\text{Ag}_2\text{S-NaA-}x$ and $\text{Ag}_2\text{S-CaA-}x$ ($x \leq 4$) are therefore mainly determined by the presence of isolated clusters and by short-range interactions between those clusters. Such local interactions are likely to be caused by two clusters located close to a window connecting adjacent α -cages.

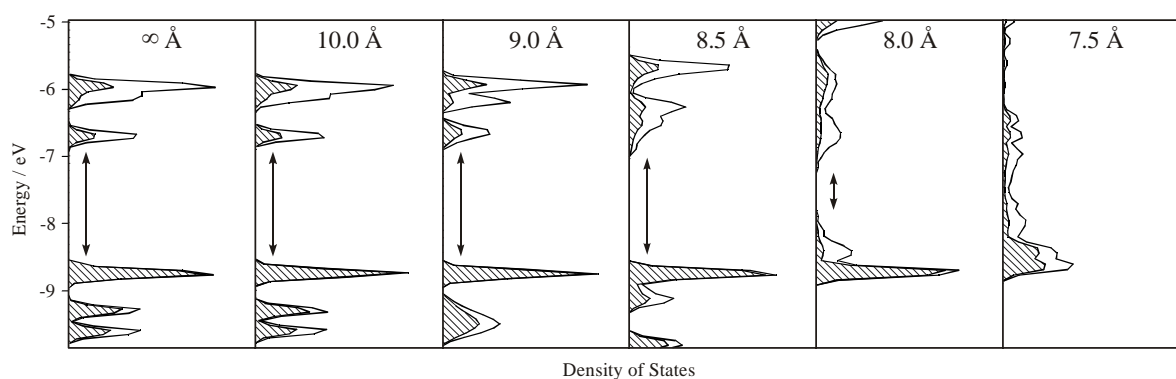


Figure 13. Density of states (DOS) of Ag_4S_2 clusters in a cubic lattice with different lattice constants. The separated system is shown on the left. The bandgap of each cluster array is marked by an arrow. The hatched region indicates the contribution of sulfur states.

5.6 Intrazeolite Charge Transport

Intrazeolite charge transport is of great practical and fundamental importance but remains a controversial topic. We focus on "classical zeolites" of which the crystalline framework can be regarded as an enormous polyanionic system containing cations for charge compensation. The intrazeolite voids may contain solvent molecules such as water, alcohol or others. In these materials the framework acts as an insulation host. This means that any charge transport is governed either by the charge compensating cations or by guests which can be molecules, ions, complexes, conducting polymers, clusters, and quantum sized particles. Different types of intrazeolite charge transport should be distinguished, depending on the transport mechanism. *Ion conductivity* is determined by the mobility of cations such as Na^+ , K^+ inside the channels [69]. We name charge transport governed by intrazeolite redox processes as *redox conductivity*. In such a process the exchange of cations with the surrounding plays a role in order to maintain charge neutrality [70, 71]. *Semiconductor conductivity* is to be expected in materials in which the guests such as nanosized particles or conducting polymers form a sufficiently well developed band structure [51]. *Metal conductivity* can occur if the band gap becomes small enough [24]. Combinations of these mechanisms are possible, depending on the composition and on the specific arrangement of the guests within the zeolite cavities.

The most delicate part for obtaining unambiguous results in charge transport experiments on zeolite materials is located at the interface. Intrazeolite charge transport on Cu^{2+} -Y zeolite, on Ag^+ -A zeolite, and on methylviologene-Y zeolite electrodes, in which the zeolite microcrystals are deposited as monolayers on glassy carbon disc electrodes, was

reported by us [71]. Baker et al. denied the importance to prepare zeolite electrodes as monolayers [72], a statement which we contradicted [71c]. He and others later focussed mainly on conditions in which the electroactivity of intrazeolite species is suppressed [73]. In the meantime impressive progress on the preparation of zeolite monolayers has been made [2-7]. We feel that any further investigations on intrazeolite charge transport should concentrate on monolayers of the best possible quality. An other approach is to investigate single nanocrystals with e.g. AFM, SEM, and confocal optical microscopy methods.

We now consider charge transport in one dimensional channels which is challenging and we present a new idea for solving the interfacial problem. The framework of zeolite L shown in Figure 14 serves as an example. The primitive vector \mathbf{c} corresponds to the channel axis while the primitive vectors \mathbf{a} and \mathbf{b} are perpendicular to it, enclosing an angle of 120° . Zeolite L crystals usually have cylindrical morphology. The number of parallel channels which coincide with the \mathbf{c} -axis of the hexagonal framework is equal to $1.07r_{\text{cyl}}^2$, where r_{cyl} is the radius of the crystal in nm. This means that a cylinder of e.g. 600 nm diameter and 300 nm length gives rise to about 100'000 parallel channels, each consisting of 400 unit cells. The channels have been filled with a large variety of molecules. This lead to materials with exciting photophysical properties, see e.g. Ref. [74].

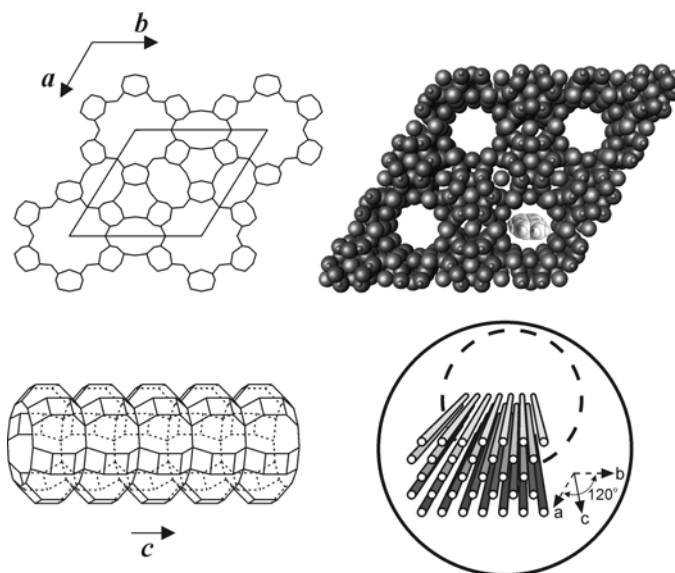


Figure 14. Framework of zeolite L. *Upper:* top view, perpendicular to the \mathbf{c} -axis, displayed as stick- (left) and as van der Waals- (right) representation with a molecule entering the zeolite channel. *Lower:* Side view of a channel along the \mathbf{c} -axis, without bridging oxygen atoms (left). Schematic view of some channels in a hexagonal zeolite crystal with cylindrical morphology.

Among the many molecules which have already been inserted into zeolite L we discuss only methyl viologen (MV^{2+}) as an example, because intrazeolite charge transport in MV^{2+} -Y zeolite electrodes has already been demonstrated [71d]. About 85 % of the unit cells can be filled with this molecule. On the basis of Rietveld refinement of X-ray data and molecular modeling, the model for the MV^{2+} location shown in Figure 15 was derived. The MV^{2+} lies along the channel wall, and the angle between the main MV^{2+} axis and the \mathbf{c} -axis of the zeolite is 27° [75]. We conclude that in such materials intrazeolite charge transfer along channels of MV^{2+} molecules is to be expected. Two problems have to be considered. Since

MV^{2+} has been entered the zeolite channel by means of ion exchange, it can leave it by the same route. This must be prevented if a stable material should result. There are several ways to do this. We have shown for Resorufin [76] that using a solvent, which cannot enter the channels of zeolites, prevents the intrazeolite molecules to exit. The latter principle has been successfully used by us in many other cases. This means that using an appropriate solvent for the electrolyte, such as polycarbonates, can solve the problem. Another possibility is the use of a conductive polymer as a closure part. The other problem lies at the electrode-zeolite interface, as stated above. We believe that it can be solved by applying the closure and stopcock molecule approach illustrated in Figure 16. It was discussed with respect to work on photonic antenna systems for light harvesting, transport and trapping [1]. First experimental evidence for its functionality in photonic antenna materials has been recently reported [77]. A stopcock generally consists of three components: a head, a spacer and a label. The tail moiety (spacer + label) has a longitudinal extension of at least one unit cell along the *c*-axis. The head has a lateral extension that is larger than the channel width and prevents the head from penetrating into the channels. The channels are therefore terminated in a general plug in like manner. Depending on the needs, stopcocks can be either applied on both sides of the cylinders or only on one side. If *redox conductivity* is envisaged, care must be taken, that the mobility of the cations, which is needed for charge compensation, is not hindered.

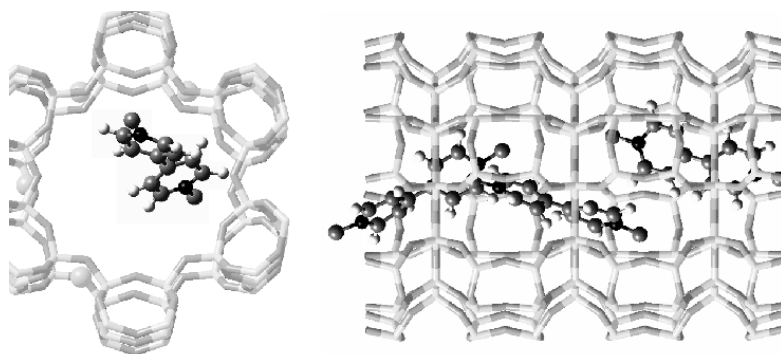


Figure 15. Location of the MV^{2+} cation inside the channel of zeolite L. Left: side view of the channel depicting a likely arrangement of the molecules along the one-dimensional channel. Right: view along the channel axis showing a position and orientation of a molecule.

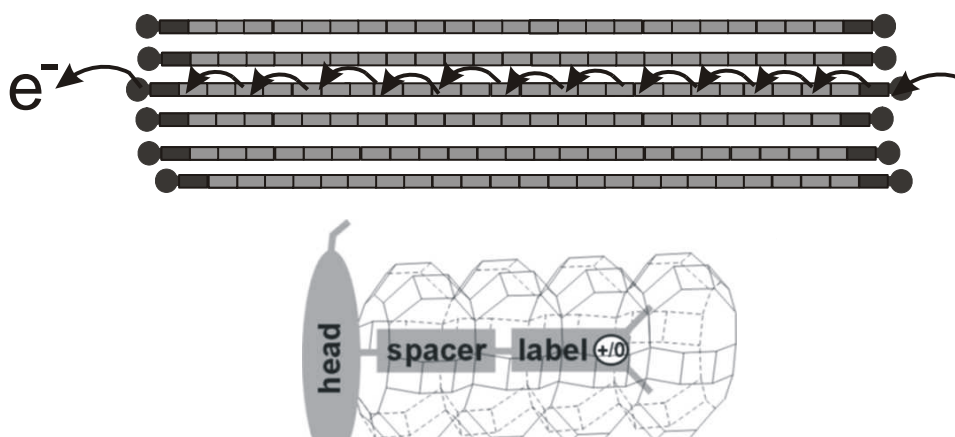


Figure 16. Principle of the stopcock approach. The channels are filled with electron conducting guests. An electron is injected on one side via the stopcock contact molecule. It travels along the channel to the other side if a corresponding voltage has been applied.

Figure 17 shows how an electrode for *redox conductivity* could look like. From this it is obvious that the success of this approach depends mainly on the skill of preparing zeolite crystals of the right morphology, of preparing monolayers on the electrode surface, and on applying the stopcock principle. It is a challenging approach and we look forward how it will develop in the near future.

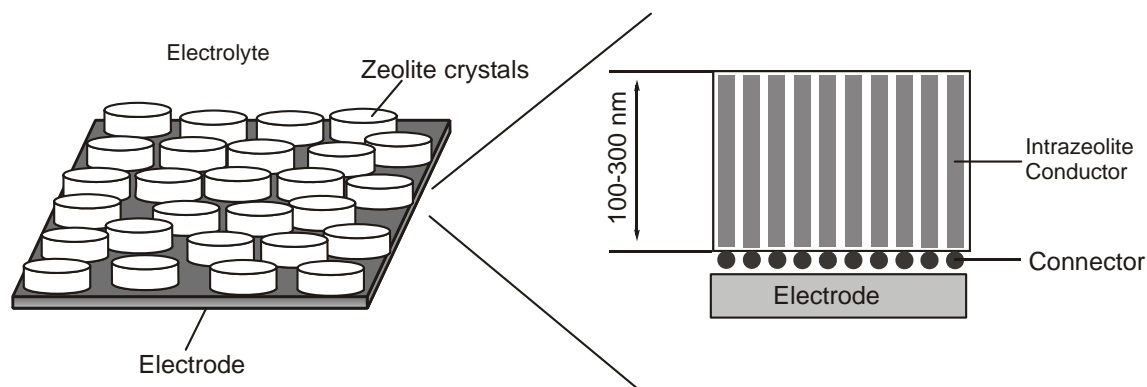
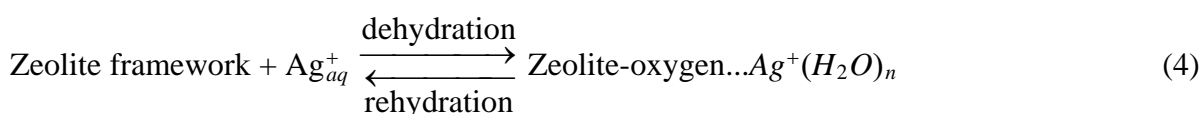
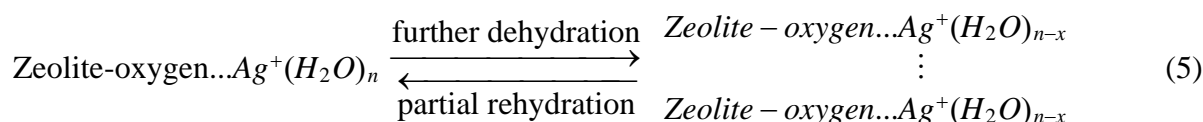


Figure 17. Principle of the stopcock-electrodes explained for hexagonal zeolite L crystals. The zeolite crystals are placed on an electrode such that contact to the electrode is made via the connector, which is the head of the stopcock. The electrode must be such that the resistance to the connector is minimized. It can e.g. consist of a conducting polymer, gold, glassy carbon and others. This principle applies similarly for a single nano- or microcrystal or for an ensemble. The connector on the electrolyte side for which several possibilities can be envisaged is not shown.

5.7 Conclusions

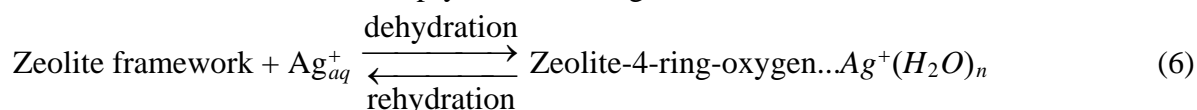
The electronic structure of a typical zeolite material can be regarded as a superposition of the electronic structure of the framework, of the charge compensating cations, of the solvent molecules, and of the guest species. The bandgap and the HOMO position of the zeolite framework are similar to those of α -quartz, despite of the fact that the material is less dense. The charge compensating cations cause new electronic states, some of which lie within the bandgap region. They can interact with each other, depending on their nature and the mean distance between them. The presence of solvent molecules, usually water, influences their interaction with the zeolite framework. The electronic structure of the zeolite framework and the charge compensating cations are not influenced by each other, if the solvation shell shields the cations from coordinating to the zeolite oxygens. A partial removal of the solvent cause incomplete saturation of the coordination shell of the cations which try to compensate this by sticking closer to the zeolite oxygens. The involved states can be perturbed considerably which causes a change of the optical properties. Silver zeolite is an excellent example, for which this perturbation can be tuned reversibly. We summarize and simplify the results reported in section 4:





The points symbolize electronic interactions between zeolite-oxygen and Ag^+ (horizontal) and between different $\text{Ag}^+(\text{H}_2\text{O})_{n-x}$ clusters (vertical).

These changes can be monitored by observing the oxygen to silver charge transfer transitions, which can be turned on and off. They are also seen in the infrared spectra. It was even possible to identify the reversible coordination of Ag^+ to the 4-ring site of zeolite A, which causes the reversible deep-yellow coloring of this otherwise colorless material [33,34]:



The extra framework cations protrude into the void internal space of zeolites. The adsorbed guest molecules are exposed to the considerable electric fields of these cations, especially in absence of solvent molecules. As a result, otherwise infrared inactive molecules like H_2 , N_2 , and O_2 are polarized and show IR spectra when embedded in a zeolite [78]. An electric field effect was used to explain the astonishing polarization of the electronic transition moments of oxonine and pyronine molecules in zeolite L, despite of the fact that the electronic absorption and fluorescence spectra of these dyes are only little influenced by the host [79]. We do not expect that such effects are important in the Ag_2S —NaA and the Ag_2S —CaA host-guest materials which consists of three-dimensional quantum dot lattices, as described in section 5. From our observations we conclude that Ag_2S and Ag_4S_2 in zeolite A and ZK4 behave as individual species with well defined properties [52]. It is remarkable that e.g. in case of Ag_4S_2 cluster materials the intercluster distances must be shorter than about 10 Å before the electronic coupling is sufficient to influence the electronic structure. This does not exclude, however, dipol-dipol and other long range coupling. — It is to be expected that not only silver sulfide cluster arrays with different structures can be produced by applying the method described in Ref. [51], but also that it can be extended to copper, gold, and other metal cations embedded in a zeolite. Comparison of different Ag_2S —zeolite composites will yield further insight into the specific interactions which govern the properties of such host-guest systems. The use of zeolite as host material opens possibilities for the assembly of highly organized macroscopic structures. Well-defined close-packed monolayers of high mechanical stability can be prepared on various substrates by using size-selected zeolite A crystals [2]. Furthermore, covalent linkage of zeolite crystals to glass supports the assembly of oriented monolayers and micro patterned structures [3,4]. Such assemblies are of special interest for the exploitation of the unique optical and electronic properties of these materials. They are of similar importance for advancing our knowledge of intrazeolite charge transport materials.

References

1. (a) G. Calzaferri, M. Pauchard, H. Maas, S. Huber, A. Khatyr, T. Schaafsma, *J. Mater. Chem.* **2002**, *12*, 1. (b) G. Schulz-Ekloff, D. Möhrke, B. van Duffel, R. A. Schoonheydt, *Micropor. Mesopor. Mater.* **2002**, *51*, 91.
2. P. Lainé, R. Seifert, R. Giovanoli, G. Calzaferri, *New J. Chem.* **1997**, *21*, 453.

3. (a) Kwang Ha, Yun-Jo Lee, Han Ju Lee, and Kyung Byung Yoon, *Adv. Mater.* **2000**, *12* (15), 1114. (b) A. Kulak, Y.-J. Lee, Y. S. Park, and K. B. Yoon, *Angew. Chem. Int. Ed.* **2000**, *39*(5), 950. (c) K. Ha, Y.-J. Lee, Y. S. Park, G. S. Lee, and K. B. Yoon, *Adv. Mater.* **2001**, *13*(8), 594. (d) K. Ha, Y.-J. Lee, D.-Y. Jung, J. H. Lee, K. B. Yoon, *Adv. Mater.* **2000**, *12*, 1614.
4. L. Huang, Z. Wang, J. Sun, L. Miao, Q. Li, Y. Yan, and D. Zhao, *J. Am. Chem. Soc.* **2000**, *122*, 3530.
5. S. Mintova, B. Schoeman, V. Valtchev, J. Sterte, S. Mo, and T. Bein, *Adv. Mater.* **1997**, *9*(7), 585.
6. S. Mintova and V. Valtchev, *Zeolites* **1996**, *16*, 31.
7. P. Yang, T. Deng, D. Zhao, P. Feng, D. Pine, B. F. Chmelka, G. M. Whitesides, G. D. Stucky, *Science* **1998**, *282*, 2244.
8. N. Herron, Y. Wang, M. M. Eddy, G. D. Stucky, D. E. Cox, K. Moller, and T. Bein, *J. Am. Chem. Soc.* **1989**, *111*, 530.
9. G. D. Stucky and J. E. Mac Dougall, *Science* **1990**, *247*, 669.
10. G. A. Ozin, M. R. Steele, and A. J. Holmes, *Chem. Mater.* **1994**, *6*, 999.
11. M. M. Garcia, H. Villavicencio, M. Hernandez-Velez, O. Sanchez, J. M. Martinez-Duart, *Materials Science and Engineering* **2001**, *C15*, 101.
12. J. R. Martin-Palma, M. Hernandez-Velez, I. Diaz, H. Villavicencio-Garcia, M. M. Garcia-Poza, J. M. Martinez-Duart, J. Perez-Pariente, *Materials Science and Engineering* **2001**, *C15*, 163.
13. X. S. Zhao, G. J. Millar, and G. Q. Lu, *J. Porous Mater.* **1996**, *3*, 61.
14. J. E. Mac Dougall, G. D. Stucky, N. Herron, Y. Wang, K. Moller, T. Bein, D. Cox, *J. Am. Chem. Soc.* **1989**, *111*, 8006.
15. Y. Wang and N. Herron, *J. Phys. Chem.* **1987**, *91*, 3257.
16. A. A. Demkov and O. F. Sankey, *J. Phys.: Condens. Matter* **2001**, *13*, 10433.
17. O. Dag, A. Kuperman, G. A. Ozin, *Adv. Mater.* **1995**, *7*(1), 72.
18. O. Dag, G. A. Ozin, H. Yang, C. Reber, and G. Bussière, *Adv. Mater.* **1999**, *11*(6), 474.
19. H.-J. Schwenn, M. Wark, G. Schulz-Ekloff, H. Wiggers, U. Simon, *Colloid Polym. Sci.* **1997**, *275*, 91.
20. X. Liu, K.-K. Iu, and J. K. Thomas, *Chem. Phys. Lett.* **1992**, *195*(2-3), 163.
21. W.-H. Zhang, J.-L. Shi, H.-R. Chen, Z.-L. Hua, and D.-S. Yan, *Chem. Mater.* **2001**, *13*, 648.
22. M. Wark, G. Schulz-Ekloff, Nils I. Jaeger, *Bulg. Chem. Comm.* **1998**, *30*(1-4), 129.
23. M. Bärtsch, P. Bornhauser, G. Calzaferri, R. Imhof, *J. Phys. Chem.* **1994**, *98*, 2817.
24. M. Brändle, G. Calzaferri, *Res. Chem. Intermed.* **1994**, *20*, 783.
25. P. Bornhauser, G. Calzaferri, *J. Phys. Chem.* **1996**, *100*, 2035.
26. G. Calzaferri, in *Tailor-made Silicon-Oxygen Compounds, From Molecules to Materials*, Eds. R. Corriu, P. Jutzi, Friedr. Viehweg, Braunschweig Ge, 1996, p.149.
27. C. Marcolli, P. Lainé, R. Bühler, G. Calzaferri, J. Tomkinson, *J. Phys. Chem.* **1996**, *101*, 1179.
28. G. Calzaferri, R. Hoffmann, *J. Chem. Soc. Dalton Trans.* **1991**, 917.
29. D. W. Turner, C. Baker, A. D. Baker, C. R. Brundle, *Molecular Photoelectron Spectroscopy*, Wiley-Interscience, London, **1970**.
30. D. L. Griscom, *J. Non-Cryst. Solids* **1977**, *24*, 155.
31. R. Beer, G. Calzaferri, I. Kamber, *J. Chem. Soc. Chem. Commun.* **1991**, 1489.
32. G. Calzaferri, R. Giovanoli, I. Kamber, V. Shklover, R. Nesper, *Res. Chem. Intermed.* **1993**, *19*, 31.

33. R. Seifert, A. Kunzmann, G. Calzaferri, *Angew. Chemie* **1998**, *110*, 1603; *Int. Edition* **1998**, *37*, 1521.
34. R. Seifert, R. Rytz, G. Calzaferri, *J. Phys. Chem. A* **2000**, *104*, 7473.
35. S. Glaus, G. Calzaferri, *J. Phys. Chem. B* **1999**, *103*, 5622-5630.
36. (a) Y.-M. Kang, B.-Z. Wan, *Catalysis Today* **1995**, *26*, 55. (b) T. M. Salama, S. Takafumi, R. Ohnishi, and M. Ichikawa, *J. Phys. Chem.* **1996**, *100*, 3688.
37. S. Bordiga, G. Turnes Palomino, D. Arduino, C. Lamberti, A. Zecchina, C. Otero Arean, *J. Mol. Catal. A: Chemical* **1999**, *146*, 97.
38. G. Spoto, A. Zecchina, S. Bordiga, G. Ricchiardi, G. Martra, G. Leofanti, and G. Petrini, *Appl. Catal. B: Environmental* **1994**, *3*, 151.
39. M. Rálek, P. Jíru, O. Grubner, H. Beyer, *Collect. Czech. Chem. Commun.* **1962**, *27*, 142.
40. T. Sun, K. Seff, *Chem. Rev.* **1994**, *94*, 857.
41. J. Baumann, R. Beer, G. Calzaferri, and B. Waldeck, *J. Phys. Chem.* **1989**, *93*, 2292.
42. G. Calzaferri, W. Suter, and B. Waldeck, *J. Chem. Soc. Chem. Commun.* **1990**, 485.
42. R. Seifert, Inauguraldissertation der philosophisch-naturwissenschaftlichen Fakultät der Universität Bern, **1999**.
43. Nanoscale Materials Special Issue, *Acc. Chem. Res.* **1999**, *32*, 387.
44. T. Vossmeier; L. Katsikas; M. Giersig; I. G. Popovic; K. Diesner; A. Chemseddine; A. Eychmüller; H. Weller, *J. Phys. Chem.* **1994**, *98*, 7665.
45. C. B. Murray; D. J. Norris, M. G. Bawendi, *J. Am. Chem. Soc.* **1993**, *115*, 8706.
46. A. van Dijken, E. A. Meulenkaamp, D. Vanmaekelbergh, A. Meijerink, *J. Lumin.* **2000**, *90*, 123.
47. J. Nanda, S. Sapra, D. D. Sarma, N. Chandrasekharan, G. Hodes, *Chem. Mater.* **2000**, *12*, 1018.
48. F. W. Wise, *Acc. Chem. Res.* **2000**, *33*, 773.
49. D. Brühwiler, R. Seifert, and G. Calzaferri, *J. Phys. Chem. B* **1999**, *103*, 6397-6399.
50. G. Calzaferri, D. Brühwiler, S. Glaus, D. Schürch, A. Currao, C. Leiggenger; *J. Imag. Sci. And Technology* **2001**, *45*, 331.
51. D. Brühwiler, C. Leiggenger, S. Glaus, G. Calzaferri, *J. Phys. Chem. B* **2002**, *106*, 3770.
52. G. Calzaferri, C. Leiggenger, S. Glaus, D. Schürch, K. Kuge, *Chem. Soc. Rev.* **2003**, *32*, 29.
53. M. Faraday, *Philosoph. Transact.* **1833**, 507.
54. R. Sadanaga, S. Sueno, *Mineral. J.* **1967**, *5*, 124.
55. S. Kitova; J. Eneva; A. Panov; H. Haefke, *J. Imaging Sci. Technol.* **1994**, *38*, 484.
56. T. Tani, *J. Imaging Sci. Technol.* **1995**, *39*, 386.
57. J. W. Mitchell, *J. Imaging Sci. Technol.* **1998**, *42*, 215.
58. E. Charlier, M. Van Doorselaer, R. Gijbels, R. De Keyzer, I. Geuens, *J. Imaging Sci. Technol.* **2000**, *44*, 235.
59. R. C. Baetzold, *J. Imaging Sci. Technol.* **1999**, *43*, 375.
60. L. Motte, M. P. Pileni, *J. Phys. Chem. B* **1998**, *102*, 4104.
61. Y.-P. Sun, J. E. Riggs, H. W. Rollins, R. Guduru, *J. Phys. Chem. B* **1999**, *103*, 77.
62. V. M. Belous, V. I. Tolstobrov, O. I. Sviridova, K. V. Chibisov, *Dokl. Phys. Chem. (Engl. Transl.)* **1982**, *262*, 75.
63. K. Akamatsu; S. Takei; M. Mizuhata; A. Kajinami; S. Deki; S. Takeoka; M. Fujii; S. Hayashi; K. Yamamoto, *Thin Solid Films* **2000**, *359*, 55.
64. H. W. Rollins, F. Lin, J. Johnson, J.-J. Ma, J.-T. Liu, M.-H. Tu, D. D. DesMarteau, Y.-P. Sun, *Langmuir* **2000**, *16*, 8031.

65. M. C. Brelle, J. Z. Zhang, L. Nguyen, R. K. Mehra, *J. Phys. Chem. A* **1999**, *103*, 10194.
66. A. Henglein, M. Gutiérrez, H. Weller, A. Fojtik, J. Jirkovský, *Ber. Bunsenges. Phys. Chem.* **1989**, *93*, 593.
67. A. A. Bagatur'yants; A. A. Safonov; H. Stoll; H.-J. Werner, *J. Chem. Phys.* **1998**, *109*, 3096.
68. D. W. Breck, *Zeolite Molecular Sieves*; John Wiley: New York, 1974.
69. (a) A. K. Jonscher, *Universal Relaxation Law*, Chelsea Dielectrics, London, **1996**. (b) R. Gerhardt, *J. Phys. Chem. Solids* **1994**, *55*, 1494. (c) T. Oghushi, S. Sato, *J. Solid State Chem.* **1990**, *87*, 95. (d) E. K. Andersen, I. G. K. Andersen, E. Skou, *Chem. Solid State Mater.* **1992**, *2*, 210.
70. (a) D.R. Rolins, *Chem. Rev.* **1990**, *90*, 867. (b) D.R. Rolins, in *Advanced Zeolite Science and Applications*, Eds. J.C. Jansen, M. Stöcker, H.G. Karge, J. Weitkamp, *Stud. Surf. Sci. Catal.* **1994**, *85*, 543.
71. (a) J.-W. Li, G. Calzaferri, *J. Electroanalytical Chemistry* **1994**, *377*, 163. (b) J.-W. Li, K. Pfanner, G. Calzaferri, *J. Phys. Chem.* **1995**, *98*, 2817. (c) J.-W. Li, K. Pfanner, G. Calzaferri, *J. Phys. Chem.* **1995**, *99*, 12368. (d) G. Calzaferri, M. Lanz, J.-W. Li, *J. Chem. Soc. Chem. Commun.* **1995**, 1313.
72. M. D. Baker, C. Senaratne, M. Mc Brien, *J. Phys. Chem.* **1995**, *99*(32), 12367.
73. C. Senaratne, J. Zhang, J. Fox, I. Burgess, and M. D. Baker, *Microporous and Mesoporous Materials* **1999**, *33*, 281.
74. G. Calzaferri, H. Maas, M. Pauchard, M. Pfenniger, S. Megelski, A. Devaux, in *Adv. Photochem.* D. C. Neckers (Ed.), Vol. 27, Wiley-VCH, **2002**, 1-50.
75. B. Hennessy, S. Megelski, C. Marcolli, V. Shklover, Ch. Bärlocher, G. Calzaferri, *J. Phys. Chem. B* **1999**, *103*, 3340.
76. D. Brühwiler, N. Gfeller, G. Calzaferri, *J. Phys. Chem.* **1998**, *102*, 2923.
77. H. Maas, G. Calzaferri, *Angew. Chem. Int. Ed.* **2002**, *41*, 2284.
78. (a) H. Förster, M. Schukdt, *J. Chem. Phys.* **1977**, *66*, 5237. (b) H. Böse, H. Förster, W. Fred, *Chem. Phys. Lett.* **1987**, *138*, 401. (c) S. Bordiga, E. Garonne, C. Lamberti, A.F. Zecchina, *Chem. Soc. Faraday Trans.* **1994**, *90*, 3367.
79. S. Megelski, A. Lieb, M. Pauchard, A. Drechsler, S. Glaus, Ch. Debus, A.J. Meixner, G. Calzaferri, *J. Phys. Chem. B* **2001**, *105*, 25.